Flooded Rice Paddy Detection Using Sentinel-1 and PlanetScope Data: A Case Study of the 2018 Spring Flood in West Java, Indonesia

Hiroyuki Wakabayashi [ID], *Member, IEEE*, Chiharu Hongo, Takahiro Igarashi, Yoshihiro Asaoka, Boedi Tjahjono, and Intan Rima Ratna Permata

Abstract—This study aims to detect flooded rice paddies in Indonesia using remotely sensed data from a relatively extensive flood that occurred in the Tegalluar area of Bojongsoang in the spring of 2018, which was observed by the Sentinel-1 and PlanetScope satellites. We propose an automatic thresholding method for the detection of flooded areas in rice paddy fields using Sentinel-1 *C*-band synthetic aperture radar (SAR) data acquisitions from before and during flooding. The flood-detection accuracy was verified using visible and near-infrared images acquired by the PlanetScope satellites. The proposed method showed that the VV (transmit V and receive V polarizations) data outperformed the VH (transmit V and receive H polarizations) data in terms of correlation ratio and discriminant accuracy. The overall classification accuracy of the nonflooded and flooded areas reached 84.7% with the VV data and 80.6% with the VH data, including the error that resulted from the time difference in the data acquired by Sentinel-1 and PlanetScope. Utilizing speckle-reducing filters with SAR data was found to improve the overall classification accuracy by 5%.

Index Terms—Agricultural insurance, flood, gamma naught, linear discriminant analysis (LDA), normalized difference water index (NDWI).

I. INTRODUCTION

THE RICE productivity of Indonesia is the third largest in the world. Rain plays an important role in the production of rice, especially in areas where the dry and rainy seasons are clearly differentiated, such as tropical Asia. However, the spatial and temporal changes in precipitation that are a result of recent climate changes have damaged crops via natural disasters, such as floods and droughts. The sustainable expansion of agricultural production is, therefore, an issue, both economically and in terms of food security. Indonesia launched an agricultural insurance system in 2016 that covers rice paddy damage resulting from natural disasters, such as floods and droughts. The insurance covers the cost of crops lost to such disasters, guaranteeing the income of farmers and allowing farmers to continue farming. The insurance, therefore, plays an essential role in expanding sustainable agricultural production. Damage assessment is necessary for calculating the payment that can be claimed by farmers as agricultural insurance.

Field surveys are currently used to evaluate the damage that has occurred to rice paddies as a result of flooding. Pest observers, damage assessors, are assigned to evaluate damage at the county level. The condition of a site is evaluated as soon as a flood retreats. This evaluation includes determination of whether future growth is possible via a visual check of the growth stage, the number of days over which flooding occurred, and the state of any remaining leaves. Rice paddy fields that are flooded within 30 days of transplanting are excluded from evaluation because replanting is possible in these fields.

The areas covered by individual pest observers can be vast and can range from 5000 to 10 000 ha, depending on the county. Observers cannot access fields that are still submerged because roads are also generally flooded when these events occur. The current evaluation process, therefore, takes significant amounts of time and is labor intensive, and associated problems in terms of time and labor shortages need to be addressed. The first step in flood damage assessment is to identify flooded areas as soon as flooding occurs. Using remotely sensed data to replace this first step could significantly reduce the workload of pest observers. The joint JICA-JST funded SATREPS research project [1]–[4], therefore, seeks a method to evaluate damage that uses remotely sensed data. SATREPS uses data from the period 2017 to 2022.

This study aims to detect flooded rice paddies in Indonesia using remotely sensed data as a part of the SATREPS project. Synthetic aperture radar (SAR) data was primarily selected for this purpose because the method can produce high-resolution data in almost all weather conditions.

Fully flooded paddies are observed as low backscatter areas in SAR images due to specular reflection. Methods to detect flooded areas using changes in backscattering have been

Hiroyuki Wakabayashi, Takahiro Igarashi, and Yoshihiro Asaoka are with the College of Engineering, Nihon University, Fukushima 963-8642, Japan (e-mail: wakabayashi.hiroyuki@nihon-u.ac.jp; ceta21001@g.nihon-u.ac.jp; asaoka.yoshihiro@nihon-u.ac.jp).

Chiharu Hongo is with the Center for Environmental Remote Sensing, Chiba University, Chiba 263-8522, Japan (e-mail: hongo@faculty.chiba-u.jp).

Boedi Tjahjono is with the Faculty of Agriculture, IPB University, Jalan Meranti - IPB Dramaga Campus, Bogor 16680, Indonesia (e-mail: boetjah@apps.ipb.ac.id).

Intan Rima Ratna Permata is with the Center for Food Crops and Horticulture Protection of West Java Province, Jalan Ciganitri II Pos Bojongsoang, Bandung 40288, Indonesia (e-mail: ambari_ayahku@yahoo.com).

Digital Object Identifier 10.1109/JSTARS.2021.3083610

successfully applied to SAR data at various frequencies [5]–[8]. This method uses a threshold to divide a region into flooded and nonflooded with lower backscatter denoting flooding and high backscatter suggesting nonflooded vegetated or non-built-up areas. Another approach to detecting flooded areas is the use of interferometric coherence calculated in interferometric SAR analysis [9], [10]. Interferometric coherence can perceive changes in the backscattering mechanisms over two periods of data acquisition, with flooded areas giving low coherence in both non-built-up and built-up areas [10]. Texture information derived from the gray-level co-occurrence matrix (GLCM) can also be used to detect flooded areas [11], [12]. Each element in the GLCM represents the relative occurrence of two different gray levels using pixels that are separated by a fixed distance, and the statistics calculated from the GLCM elements provide quantitative textural information [13]. Using a combination of both backscattering and textural information can improve the accuracy of flood detection [12].

This study investigates Sentinel-1 SAR data from a test site in Indonesia to detect the areas that were flooded during the rainy season in 2018. PlanetScope satellite images were used to verify the results of extracting the flooded area by comparing the classification results obtained from both the SAR-based and the optical sensor-based methods.

II. TEST SITE

Indonesia often experiences flooding. Based on the data from the National Disaster Management Agency (BNPB), 7106 flood events occurred during the period from 2000 to 2016, with floods occurring in all provinces. West Java Province often experiences flooding, especially Bandung Regency, where flooding occurs each year when Citarum River overflows. This is especially prevalent in the rainy season and the three subdistricts Bojongsoang, Baleendah, and Dayeuhkolot, which are often submerged as a result of flooding. These flood events lead to significant physical, economic, and social impacts for the residents of Bandung Regency [14].

Bojongsoang County was used as a test site in this research. The county is located approximately 4 km southeast of Bandung City in West Java province. The area is one of those in which SATREPS is developing damage assessment methods for agricultural insurance. The Citarum River flows along the eastern and southern boundaries of Bojongsoang, and the adjacent paddy fields are often flooded during the rainy season from December to April. According to the pest observer in Bojongsoang, an extensive flood occurred at the center of Tegalluar, located in eastern Bojongsoang, from February 20, 2018 to March 10, 2018.

Fig. 1 shows a land-use map of Bojongsoang County that was created at IPB University [14]. The map was produced from a visual interpretation of the QuickBird imagery available on Google Earth Pro and verified in the field. Rice paddy fields cover approximately 63% of the land area with lesser proportions comprising settlements, buildings, and residential areas.
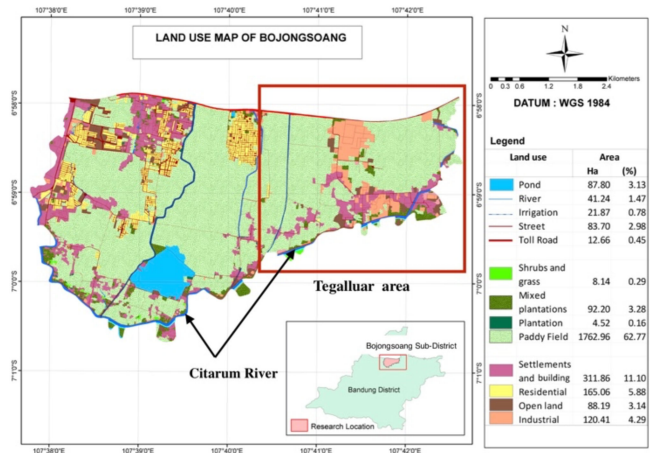

Fig. 1.　Land-use map of Bojongsoang.

TABLE I
CHARACTERISTICS OF THE SENTINEL-1 C-BAND
SAR IW-MODE GRD PRODUCT

Satellite	Sentinel-1A (IW mode)
Center frequency (wave length)	5.405 GHz(5.6 cm)
Ground range coverage	251.8 km
Incidence angle	29.1 - 46.0 deg.
Number of sub-swath	3
Spatial resolution (range x azimuth)	20.3 - 20.5 m × 22.5-22.6 m
Number of looks (range x azimuth)	5 × 1
Equivalent number of looks	4.3-4.4 (varied with scan)
Pixel spacing (range x azimuth)	10m × 10m
Polarization	VV+VH

III. REMOTE SENSING DATA

A. Sentinel-1 SAR Data

Sentinel-1 C-band SAR data were used to detect flooded rice paddy fields because it can obtain relatively high-resolution data in almost all weather conditions. SAR data with ascending orbits in the interferometric wide (IW) swath mode were obtained for the study area on February 17 and March 1 [15]. The IW mode employs the terrain observation with progressive scans SAR technique [16] to acquire data over a 250-km swath with a spatial resolution of approximately 20 m. The ground range detected (GRD) data were used for our analysis. Table I summarizes the characteristics of the IW-mode GRD product on Sentinel-1 [17], [18]. The incidence angle at the center of the Tegalluar area was approximately 43°. Both VV (transmit V and receive V polarizations) and VH (transmit V and receive H polarizations) polarization data were used in this study.

B. PlanetScope Image

PlanetScope satellite images were used to evaluate the accuracy of the flood detection with Sentinel-1 SAR data. Because the PlanetScope satellite constellation consists of more than 130

TABLE II
CHARACTERISTICS OF PLANETSCOPE IMAGE

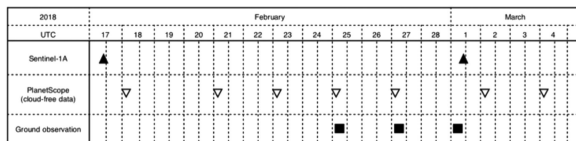| Satellite	PlanetScope
Orbit altitude	475 km
Equator crossing time	9:30 - 11:30 am
Ground sampling distance (nadir)	3.7 m
Spectral bands	Blue: 464-517 nm Green: 547-585 nm Red: 650-682 nm NIR: 846 -888 nm
Pixel spacing (Level 3B product)	3 m
Bit depth (Level 3B product)	16 bit

Fig. 2. Timeline of data acquisitions made by Sentinel-1 and PlanetScope satellite for Tegalluar in east Bojongsoang from February 17, 2018 to March 4, 2018. The figure includes the period over which ground observations were made, which were conducted three times during the flooding period.
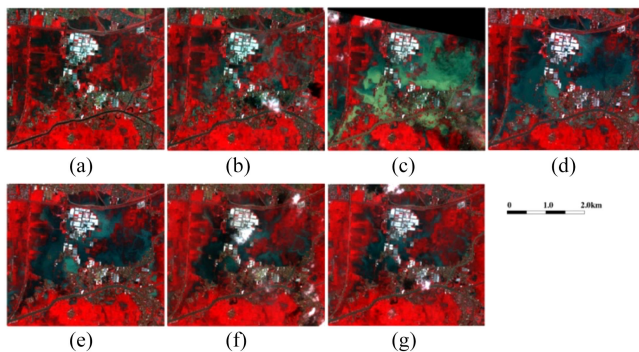

Fig. 3. Series of false-colored PlanetScope images covering Tegalluar in east Bojongsoang acquired from February 18, 2018 to March 4, 2018. (a) 02:33 UTC on February 18, 2018. (b) 02:32 UTC on February 21, 2018. (c) 02:32 UTC on February 23, 2018. (d) 03:47 UTC on February 25, 2018. (e) 02:32 UTC on February 27, 2018. (f) 02:34 UTC on March 02, 2018. (g) 02:33 UTC on March 04, 2018. The upper frame of image (c) was partially lost.

active satellites [19], images of a specific land surface can be acquired for most days. The on-board sensor has four visible and near-infrared bands with a pixel spacing of 3 m. Table II summarizes the characteristics of the PlanetScope images. Level 3B products, or the "PlanetScope ortho scene product," were used for our analysis. These products are processed, orthorectified, and scaled top of atmosphere radiance image products that are suitable for both analysis and visual application [20]. This product has scene-based framing and is projected onto a cartographic projection in the GeoTiff format.

Seven cloud-free images were obtained for the period in which the 2018 flood event occurred. Fig. 2 summarizes a timeline of the data acquired by the Sentinel-1A and PlanetScope satellites. Fig. 3 shows a series of false-colored images for the entire

Tegalluar area that were taken by the PlanetScope satellites from February 18, 2018 to March 4, 2018. The RGB on the false-colored image assigns the NIR, red, and green channels. False-colored images are often used to interpret land vegetation cover, meaning that it was possible to visually recognize the increase and decrease in the area flooded from these time-series images. The pest observer in Bojongsoang did not report any flooding in the Tegalluar area during mid-February 2018. The interpretation of the images indicates that the flood began encroaching the center of Tegalluar on February 21 [see Fig. 3(b)], expanded over the period February 23 [see Fig. 3(c)] to February 27 [see Fig. 3(e)] and started to shrink on March 2 [see Fig. 3(f)].

IV. DATA PROCESSING AND FLOOD DETECTION

A. Flood Area Detection Methods With SAR Data

Since Sentinel-1 SAR data for both before and during the flood were available, it was possible to use both backscattering and the interferometric approach to detect the changes in scattering that are caused by flooded rice paddies. First, the backscattering and the coherence images of the test site were compared. Although the change in the backscattering was easily recognized, differences in the coherence were not easily observed. The average coherence of the rice paddies in Tegalluar was low at 0.32, with a baseline of +16.1 m. The backscattering approach was, therefore, selected for this study.

Many methods have been proposed for optimizing the backscatter threshold used, such as the split-based automatic thresholding procedure that is applied to TerraSAR-X data [21], a combination of image segmentation and the surface scattering model that is applied to CosmoSkyMed *X*-band SAR data [22], and a threshold that maximizes the kappa coefficient that is applied to PALSAR-2 data [23]. The common idea involved in these methods is to optimize the threshold via consideration of the land surface and the incidence angle. This is because backscattering is usually related to these parameters.

Because this study aims to use remotely sensed data to obtain a damage evaluation for agricultural insurance, a simple implementation method is required and lower computational costs are preferable. We, therefore, investigated the automatic determination of an optimal threshold. The gamma naught (gamma-0:γ^0) was used instead of the backscattering coefficient (σ^0) to reduce the sensitivity to the incidence angle when determining a threshold. For flat areas, such as our test site and rice paddy fields, the relationship between γ^0 and σ^0 is given by a simple equation

$$\gamma^0 = \frac{\sigma^0}{\cos\theta} \tag{1}$$

where θ is the ellipsoidal incidence angle of the Earth. The derived threshold can then be easily converted into a σ^0 threshold.

Automatic threshold determinations based on the statistical methods described in the Kittler and Illingworth (KI) [26] and Otsu's approaches [27] have previously been applied to the *C*- and *X*-band SAR data for flood detection [6], [22], [24], [25]. Otsu's approach was used in this study because of its rapidity and robustness with bimodal distributions.
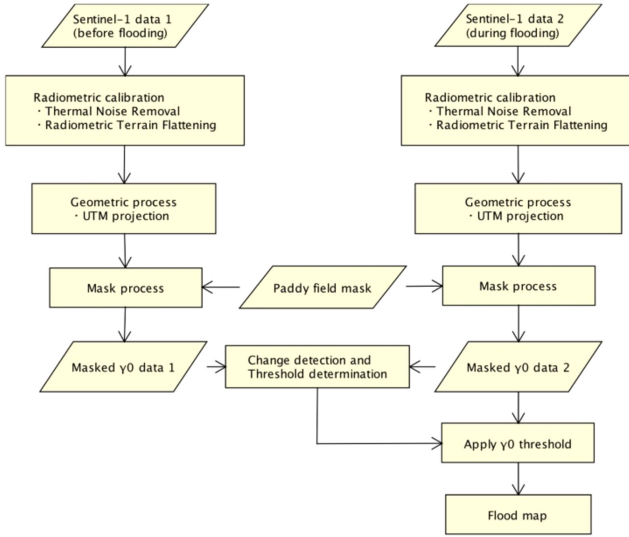
Fig. 4.   Proposed procedure used to extract flooded areas using Sentinel-1 SAR data.

Fig. 5.   Sentinel-1 γ^0 images of the test site. (a) and (b) VV and VH images acquired at 11:15 UTC on February 17, 2018. (c) and (d) VV and VH images acquired at 11:15 UTC on March 1, 2018.

B. Proposed Method for Change Detection and Automatic Thresholding With SAR Data

Level-1 GRD data were downloaded from the European Space Agency Copernicus Open Access Hub and input into the Sentinel Toolbox software [28] for further analysis. Fig. 4 shows the procedure that was used to extract the flood areas from the Sentinel-1 SAR data. Each SAR dataset used was radiometrically calibrated to γ^0 and projected onto the UTM coordinates (Zone S48). The shuttle radar topography mission digital elevation model with a 1-arc-sec (30 m) grid was applied to both radiometric terrain flattening [29] and orthorectified processing. The pixel spacing on the UTM coordinates was set to 10 m [17] in consideration of the size of the rice paddies at the test site. Fig. 5 shows the Sentinel-1 γ^0 orthorectified images that were acquired for the test site on February 17, 2018 and March 1, 2018.

As the final goal of this study was to extract the fully flooded paddy fields, the area outside the rice paddy fields was excluded using the data from the land-use map in Fig. 1. Because flooded rice paddy fields usually have a lower γ^0 than nonflooded areas, our change detection method utilizes the difference in the value of $\gamma°$ for two classes describing the nonflooded and the flooded paddy fields. Sites, where the difference in the value of γ^0 was greater than a predetermined threshold, were detected (preset difference: $\delta_{\gamma 0}$) and γ^0 samples that satisfied the following equation were extracted:

$$\gamma^0_1 - \gamma^0_2 \geqslant \delta_{\gamma^0} \qquad (2)$$

where $\gamma^0{}_1$ and $\gamma^0{}_2$ denote the γ^0 samples extracted in the nonflooded and flooded situations, respectively.

Next, Otsu's thresholding was applied to determine the γ^0 value by dividing the two classes with the maximum between-class variance [27]. Sample histograms from both classes with apparent bimodal distributions were used to determine the threshold for the two classes. Finally, the flooded paddy fields were extracted using the γ^0 threshold, as shown in Fig. 4.
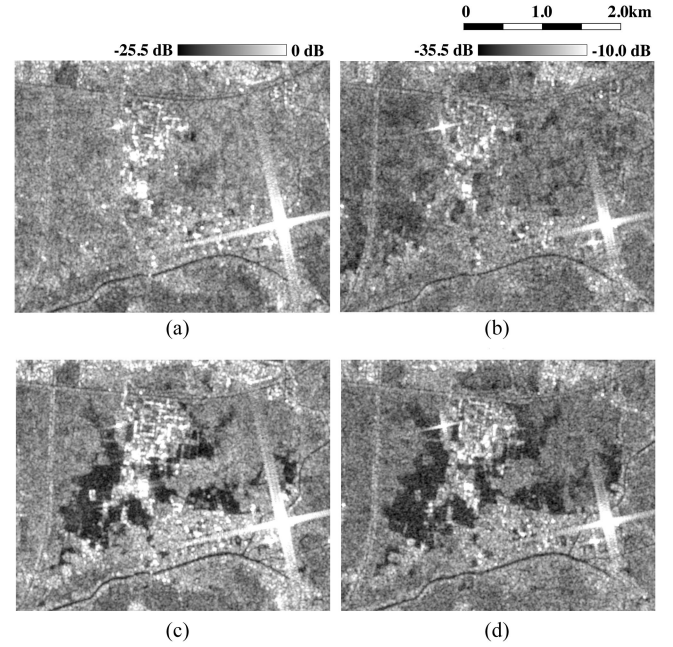
C. Flood-Detection Methods With PlanetScope Image

The PlanetScope satellite image includes four bands in the visible and near infrared with 3 m pixel spacing, as given in Table II. The normalized difference water index (NDWI) was used to detect flooded areas on the PlanetScope image. The NDWI was proposed by McFeeters [30] and was calculated from the green and near-infrared bands. The NDWI can be used to delineate and enhance the presence of water bodies and is calculated using the following:

$$\text{NDWI} = \frac{R_g - R_n}{R_g + R_n} \qquad (3)$$

where R_g and R_n represent the reflectances in the green and near-infrared bands, respectively. The reflectance of each band was calculated from the orthoscene (level 3B) products using the scaling coefficient [20]. Fig. 6 shows the calculated NDWI images that were created using the PlanetScope satellite images. The images were resampled to the UTM coordinate system (Zone S48) with 10 m pixel spacing to compare the flood detected with the Sentinel-1 results. These images can, therefore, be used to directly assess the flooded areas that are extracted from the Sentinel-1 data.

Linear discriminant analysis (LDA) was then applied to determine the NDWI threshold between the nonflooded and flooded areas. First, the within-class and between-class variance of the two classes associated with nonflooded and flooded paddy fields that were recognized in the PlanetScope images was determined. The data acquired on February 18 were used as nonflood samples, while data from February 25 were designated as the flood samples. These dates were used because the flood was known
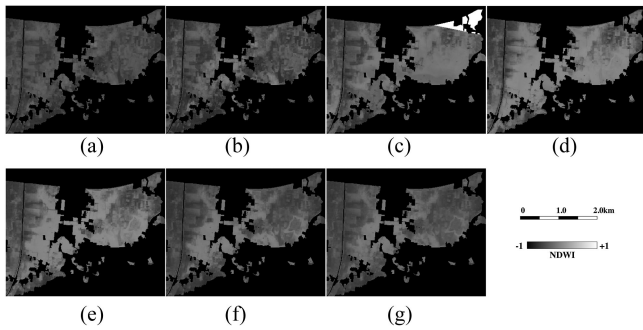
Fig. 6. Series of NDWI images covering Tegalluar in east Bojongsoang acquired during the period February 18, 2018 to March 4, 2018. (a) February 18, 2018. (b) February 21, 2018. (c) February 23, 2018. (d) February 25, 2018. (e) February 27, 2018. (f) March 2, 2018. (g) March 4, 2018. These images were resampled to the UTM coordinate system (Zone S48) with a pixel spacing of 10 m. The upper frame of image (c) was partially lost.

Fig. 8. Series of the flooded area detected from February 18, 2018 to March 4, 2018 using the NDWI threshold. (a) February 18, 2018. (b) February 21, 2018. (c) February 23, 2018. (d) February 25, 2018. (e) February 27, 2018. (f) March 2, 2018. (g) March 4, 2018. The upper frame of image (c) was partially lost.
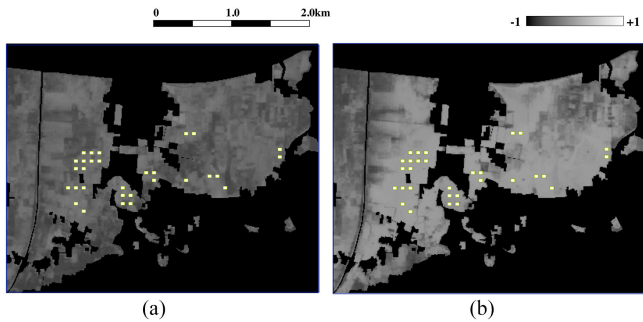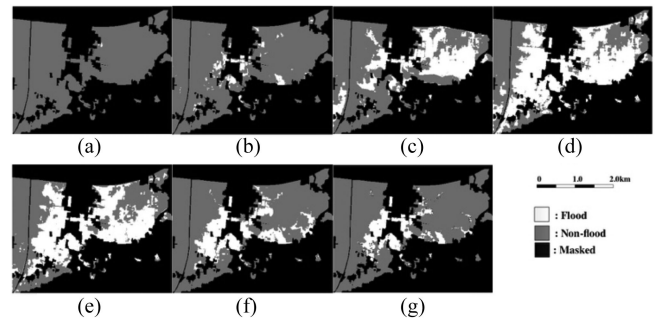

Fig. 7. Sampling points in the Tegalluar area plotted onto the NDWI images. (a) February 18, 2018. (b) February 25, 2018. A total of 30 sampling points were used. Since 3 × 3 pixels were centered at each point, a total of 270 nonflood and flood samples were produced.
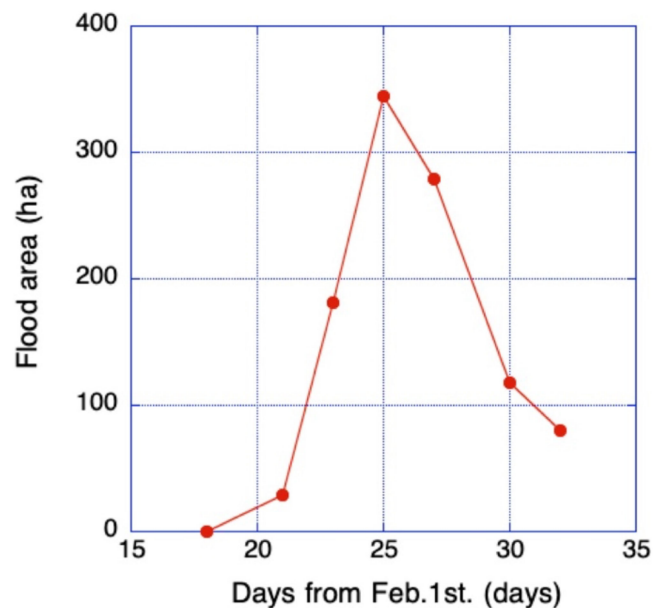
Fig. 9. Calculated flooded areas based on the results of Fig. 8.

to have started after February 18 and was at a maximum on February 25.

The total variance (S_t) is the sum of the between-class variance (S_b) and within-class variance (S_w). We can define the correlation ratio (η) using

$$\eta = \frac{S_b}{S_t}. \qquad (4)$$

The parameter η can be used as an index to describe the separation between classes from the LDA. In other words, the point at which two classes can be separated is determined by maximizing η [31].

Fig. 7 shows the sampling points that were used to determine the NDWI thresholds from a total of 270 samples. The determined NDWI threshold was 0.0236 with a correlation ratio of 0.941. This threshold was, thus, applied to all the NDWI images to generate information about the area that was flooded each day, as shown in Fig. 8. Fig. 9 shows the changes in the flooded areas that were calculated from Fig. 8. Flooding continued increasing in the test site until February 25, after which it decreased. The maximum flooding reached more than 300 ha on February 25.

V. RESULTS AND DISCUSSIONS

A. Result of γ^0 Thresholding

The SAR backscattering coefficients can decrease in all polarizations when a full flood occurs in a rice paddy field. The dominant backscattering mechanism changes from double bounce and volume scattering (partially flooded paddies) to specular reflection (fully flooded paddies) as the water level increases. Because the threshold for the backscattering coefficient can successfully be used to classify flooded and nonflooded areas using various SAR frequencies [5]–[7], this methodology can also be used for the *C*-band SAR data produced by Sentinel-1. Following the procedure, as indicated in Fig. 4, flood detection was carried out using the Sentinel-1 SAR γ^0 data acquired on February 17, 2018 and March 1, 2018, using γ^0 sample data for both nonflooded and flooded conditions to determine the threshold between the two groups.

Fig. 10. Number of extracted samples with $\delta_{\gamma 0}$.

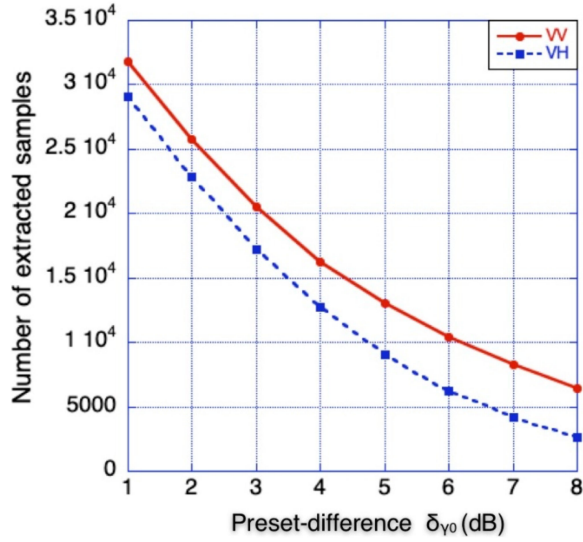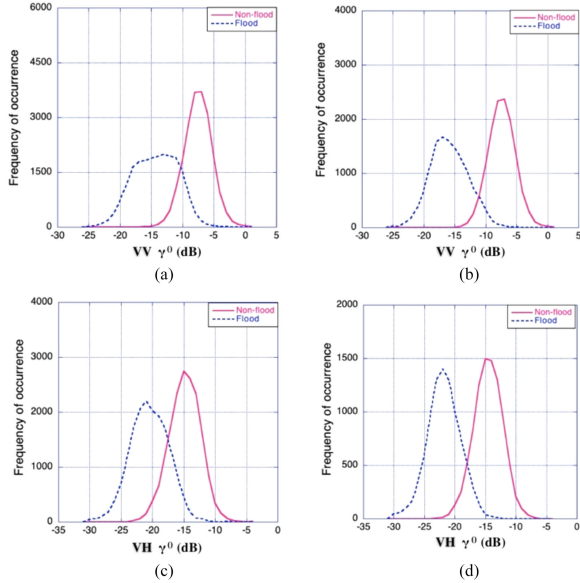Fig. 11. Histograms of γ^0 samples extracted from both nonflooded (February 17) and flooded (March 1) rice paddy fields. (a) VV $\delta_{\gamma 0} = 3$ dB. (b) VV $\delta_{\gamma 0} = 5$ dB. (c) VH $\delta_{\gamma 0} = 3$ dB. (d) VH $\delta_{\gamma 0} = 5$ dB.

Fig. 12. Flooded area detected using the γ^0 thresholds given in Table III. (a) VV (b) VH.

TABLE III
RESULT OF DERIVED γ^0 THRESHOLDS FOR BOTH VV AND VH POLARIZATION DATA

Polarization	Thresholds(dB)	η(Sb/St)	Discriminant accuracy (%)
VV	-12.68	0.778	93.3
VH	-18.93	0.743	92.0

TABLE IV
CONFUSION MATRICES FOR THE RESULTS OF THE NONFLOOD AND FLOOD CLASSIFICATION WITH A NONFILTERED γ^0 (OA: OVERALL ACCURACY, PA: PRODUCER ACCURACY, AND UA: USER ACCURACY)

	NDWI (3/2)				
	Classes	Flood	Non-flood	Row total	UA(%)
VV	Flood	9,631	7,248	16,879	57.1
γ^0	Non-flood	2,190	42,425	44,615	95.1
(3/1)	Column total	11,821	49,673	61,494	
	PA (%)	81.5	85.4	OA(%)	84.7
				Kappa(%)	57.6
	Classes	Flood	Non-flood	Row total	UA(%)
VH	Flood	9,696	9,790	19,486	49.8
γ^0	Non-flood	2,125	39,883	42,008	94.9
(3/1)	Column total	11,821	49,673	61,494	
	PA (%)	82.0	80.3	OA(%)	80.6
				Kappa(%)	50.0

To obtain γ^0 samples for nonflooded and flooded rice paddy fields, a simple change detection method was adopted that uses the difference between two groups. The data acquired on February 17 were used as nonflooded samples, while those from March 1 were considered as flooded samples. Samples from areas in which the value of γ^0 was significantly different from the preset $\delta_{\gamma 0}$ were then extracted.

Trials were then conducted in an attempt to change the $\delta_{\gamma 0}$ from 1 to 8 dB in 1 dB increment. Fig. 10 shows the number of samples extracted with the preset difference. As expected, the number of sample data decreased as the preset value increased. Fig. 11 shows the examples of the γ^0 distributions (histograms) that were extracted from both nonflooded and flooded rice paddy
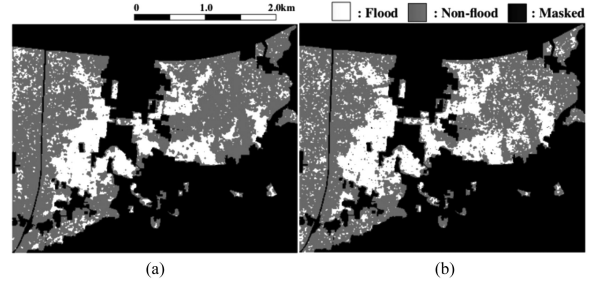
fields. The γ^0 distribution of the flood samples was rendered unimodal by setting $\delta_{\gamma 0}$ to > 5 dB for the VV and VH polarizations. Considering the number of samples and the shape of the γ^0 sample distribution, 5 dB was adopted as the value of $\delta_{\gamma 0}$ for the following analysis.

Table III presents the thresholds derived for VV γ^0 and VH γ^0 together with the correlation ratios and discriminant accuracy. The correlation ratio is the ratio of between-class variance to the total variance, and discriminant accuracy is the ratio of correctly detected samples to total samples. The results show that VV is slightly better than VH in terms of detection. Fig. 12 shows flooded area detected using the γ^0 thresholds given in Table III. To quantitively compare the nonflooded and flooded areas derived by Sentinel-1 with those derived by the PlanetScope images, the classification results were evaluated alongside the γ^0 thresholds using the NDWI threshold as a reference. Table IV lists the confusion matrices and the classification accuracies. The

TABLE V
DERIVED γ^0 THRESHOLDS USING LEE- AND MEDIAN-FILTERED DATA

Polarization	Filtering size	Lee filter			Median filter		
		Threshold(dB)	η(Sb/St)	Discriminant accuracy(%)	Threshold(dB)	η(Sb/St)	Discriminant accuracy(%)
VV	3x3	-12.58	0.806	95.3	-12.63	0.818	95.9
	5x5	-12.58	0.813	95.6	-12.64	0.850	98.0
	7x7	-12.51	0.815	95.8	-12.64	0.867	98.7
VH	3x3	-18.85	0.770	94.1	-18.81	0.791	95.0
	5x5	-18.83	0.779	94.4	-18.93	0.837	97.3
	7x7	-18.83	0.781	94.6	-18.95	0.867	98.5

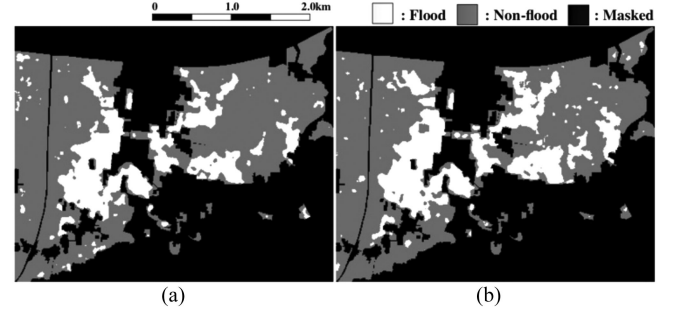Filtering size was increased from 3 to 7.

Fig. 13. Detected flood area using the 5×5 median-filtered γ^0 thresholds, as given in Table V. (a) VV. (b) VH.

TABLE VI
CONFUSION MATRICES FOR THE NONFLOOD AND FLOOD CLASSIFICATION RESULTS BY 5×5 MEDIAN-FILTERED γ^0 (OA: OVERALL ACCURACY, PA: PRODUCER ACCURACY, AND UA: USER ACCURACY)

		NDWI (3/2)			
	Classes	Flood	Non-flood	Row total	UA(%)
VV γ^0 (3/1)	Flood	9,748	4,502	14,250	68.4
	Non-flood	2,073	45,171	47,244	95.6
	Column total	11,821	49,673	61,494	
	PA (%)	82.5	90.9	OA(%)	89.3
				Kappa(%)	68.1
	Classes	Flood	Non-flood	Row total	UA(%)
VH γ^0 (3/1)	Flood	9,980	6,746	16,726	59.7
	Non-flood	1,841	42,927	44,768	95.9
	Column total	11,821	49,673	61,494	
	PA (%)	84.4	86.4	OA(%)	86.0
				Kappa(%)	61.2

overall accuracies reached 84.7% for the VV γ^0 and 80.6% for the VH γ^0. This evaluation includes the errors that resulted from the different times at which the Sentinel-1 and PlanetScope data were acquired, with a difference of approximately 15 h.

Both Sentinel-1 (March 1) and PlanetScope (March 2) acquired their data during the period in which the area flooded was shrinking, as shown in Figs. 8 and 9. Since the time difference between Sentinel-1 and PlanetScope acquisitions was approximately 15 h, a wider area was flooded when the Sentinel-1 data were acquired than when PlanetScope obtained data. Both the VV and VH flooded areas observed by Sentinel-1 were more extensive than the flooded area detected by PlanetScope in Table IV.

B. Effect of Speckle-Reducing Filters

Because the GRD data from the Sentinel-1 IW mode are processed with five multilooks in the range direction [18], the amplitude data have speckle noise with its equivalent number of looks (ENL). In this section, we investigate the effect that speckle-reducing filters have on the accuracy in terms of flood detection. The Lee and median filters were applied to reduce the speckle noise in the VV γ^0 and VH γ^0 data. The Lee filter replaces the central pixel value with a value that is estimated using the least squares method in the local window [32]. We used 4.4 as the ENL (IW3) with the Lee filter, as the ENL is required to estimate the theoretical noise level of speckle when this filter is used. After the speckle-reducing filters were applied to the VV γ^0 and VH γ^0 data, the γ^0 thresholds were estimated by the procedure, as shown in Fig. 4.

Table V summarizes the results of our analysis using the Lee and median filters of various sizes. Increasing the size of both types of filters resulted in improvements. Comparing the correlation ratio and the discriminant accuracy indicates that the median-filtered γ^0 outperforms the Lee-filtered γ^0. We, therefore, chose the median filter for application to the GRD data as a preprocessing step before the flooded area was extracted. Since increasing the filtering size causes spatial degradation, a filtering window size of 5 was used. Fig. 13 shows the flooded area detected using the 5×5 median-filtered VV γ^0 and VH γ^0 thresholds, as given in Table V. As given in Table VI, the overall classification accuracy reached 89.3% with VV γ^0 and 86.0% with VH γ^0, which is an improvement of 5% compared with the nonfiltered γ^0 results (see Table IV).

C. Flood Area Verification by Ground Observation

The *in situ* observations were conducted on both February 25 and 27 and March 1. The center of Tegalluar could not be accessed on the dates selected in February because the flooding was too extensive and ground observation was only possible at the western boundary of Tegalluar. Fig. 14 shows ground photos (panoramic images centered in a northerly direction) that were taken at precisely the same location on February 25 and February 27. These observations indicated that the paddy fields were fully flooded on February 25 and that the water depth slightly decreased on February 27. The photos verified the flooding detected using the PlanetScope images.

Fig. 15 shows ground photos that were taken by the pest observer in Bojongsoang on March 1 in 2018. It is difficult to delineate details about the area that was flooded from these photos. However, both fully flooded and partially flooded areas can be recognized. The photos were compared with the flooding detected by Sentinel-1 on March 1, which verified the accuracy of the extracted area that was considered flooded.

D. Discussion on Thresholding and Learning-Based Classification

Our proposed method for flooded rice paddy detection combines change detection and thresholding, as shown in Fig. 4.
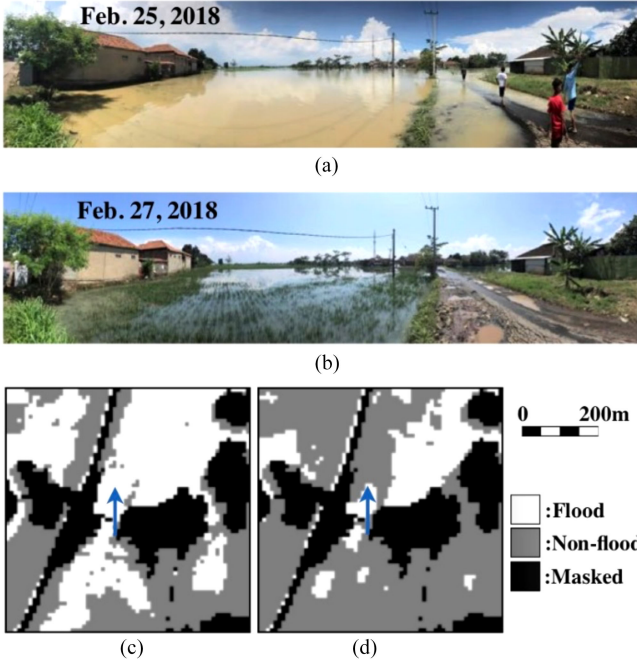
Fig. 14. Ground photos taken at the western boundary of Tegalluar on February 25 and February 27. (a) Panoramic photos taken on February 25 and (b) February 27. (c) Location and direction of the flooded area detected by PlanetScope on February 25 and (d) February 27.
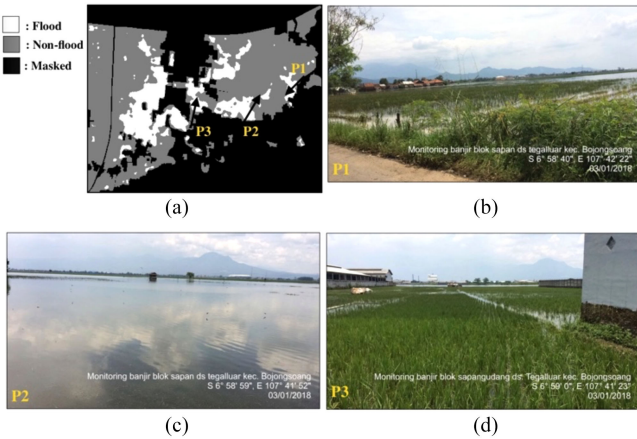

Fig. 15. Sample ground photos taken on March 1 in the Tegalluar area. (a) Ground photo locations and directions describing the area flooded by extraction of the data from Sentinel-1. (b) Location 1. (c) Location 2. (d) Location 3.

Otsu's method was used to determine the γ^0 value to classify the two classes. In this section, we compare our proposed method with other thresholding methods. The KI approach derives a threshold that minimizes the criterion function selected for the best discrimination of two Gaussian distributions [26]. The KI approach has been successfully applied to TerraSAR-X data for automated flood detection [6], [21].

The sampling datasets used in Section V-A and B were applied to determine the thresholds using the KI approach. Table VII lists the thresholds for the nonfiltered dataset, and Table VIII lists the thresholds for the filtered dataset. By comparing Tables III and

TABLE VII
RESULT OF DERIVED γ^0 THRESHOLDS BY KI APPROACH USING NONFILTERED DATA

Polarization	KI Thresholds(dB)	η(Sb/St)	Discriminant accuracy (%)
VV	-12.68	0.778	93.3
VH	-18.85	0.743	92.0

TABLE VIII
RESULT OF DERIVED γ^0 THRESHOLDS BY KI APPROACH USING FILTERED DATA

Polarization	Filtering size	Lee filter			Median filter		
		KI Threshold(dB)	η(Sb/St)	Discriminant accuracy(%)	KI Threshold(dB)	η(Sb/St)	Discriminant accuracy(%)
VV	3x3	-12.33	0.805	95.6	-12.55	0.818	96.0
	5x5	-12.33	0.813	95.9	-12.14	0.848	98.4
	7x7	-12.35	0.814	96.1	-11.84	0.864	99.5
VH	3x3	-18.78	0.770	94.2	-19.29	0.789	94.3
	5x5	-18.97	0.779	94.3	-19.26	0.835	96.8
	7x7	-19.04	0.780	94.3	-19.08	0.867	98.4

TABLE IX
COMPARISON OF CLASSIFICATION ACCURACIES BETWEEN OTSU'S METHOD AND KI APPROACH WITH NONFILTERED AND 5 × 5 MEDIAN-FILTERED γ^0 (OA: OVERALL ACCURACY, NF: NONFILTERED, AND MED: MEDIAN FILTERED)

Input data		Proposed (Otsu)		KI	
		OA(%)	Kappa(%)	OA(%)	Kappa(%)
NF	VV	84.7	54.6	84.7	54.6
	VH	80.6	50.0	80.0	48.9
Med	VV	89.3	68.1	87.3	64.2
	VH	86.0	61.2	86.5	62.0

V with Tables VII and VIII, we found that the derived threshold difference obtained by the two methods was <0.5 dB.

Otsu's and KI methods use different approaches to determine their thresholds. Otsu's method maximizes the between-class variance (correlation ratio), and the KI approach minimizes the criterion function selected under the assumption of dividing two Gaussian distributions. By comparing Table V with Table VIII, we can recognize that Otsu's method provides a better correlation ratio than the KI approach, proving the difference between the two methods. Although the KI approach provides slightly higher discriminant accuracy in Table VIII (7 out of 12), this result corresponds to the accuracy of the sampled data. Table IX presents the accuracy comparison between Otsu's method and the KI approach, derived from confusion matrices for the nonflooded and flooded classification results with nonfiltered and median-filtered γ^0 data. Otsu's method yields the highest overall accuracy and Kappa with the median-filtered VV data and obtains better accuracies, except for the median-filtered VH data.

We also compared the proposed method with a learning-based algorithm. The support vector machine (SVM) is a supervised learning algorithm that focuses on training samples closest to an optimal boundary between the feature space classes [33]. The strategy used by this algorithm is to maximize the distance between the training samples and the discrimination boundary and improve the generalization performance. SVM is widely used

TABLE X
LIST OF DERIVED SVM CLASSIFIER WITH NONFILTERED AND 5×5 MEDIAN-FILTERED γ^0 (NF: NONFILTERED AND MED: MEDIAN FILTERED)

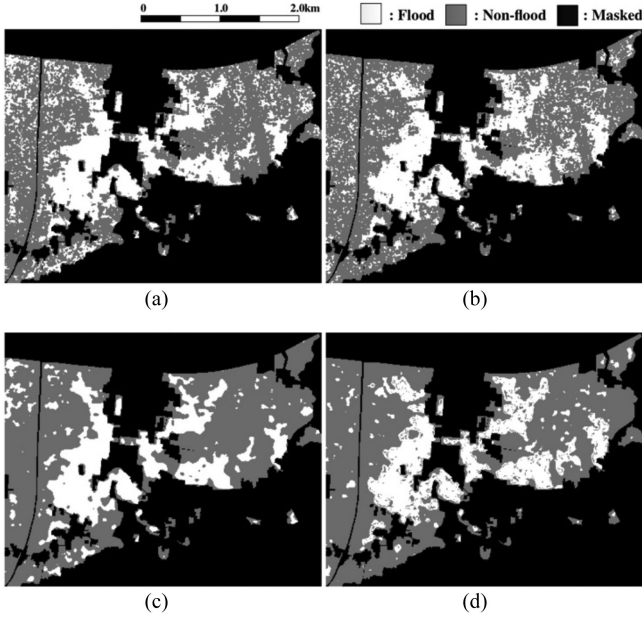| Input data		No. of training samples	hyperparameters		Discriminant accuracy(%)
			cost	gamma	
NF	VV	12,998	2^7	2^{-10}	94.7
	VH	9,062	2^{15}	2^0	92.5
Med	VV	11,179	2^{15}	2^{-10}	98.7
	VH	6,266	2^{13}	2^{10}	97.6

Fig. 16. Detected flood area using SVM classifier with nonfiltered and filtered γ^0 data. (a) Nonfiltered VV. (b) Nonfiltered VH. (c) 5×5 median-filtered VV. (d) 5×5 median-filtered VH.

TABLE XI
CONFUSION MATRICES FOR NONFLOOD AND FLOOD CLASSIFICATION RESULTS BY SVM WITH NONFILTERED AND 5×5 MEDIAN-FILTERED γ^0 (OA: OVERALL ACCURACY, PA: PRODUCER ACCURACY, UA: USER ACCURACY, NF: NONFILTERED, AND MED: MEDIAN FILTERED)

	NDWI (3/2)				
VV γ^0 (3/1) NF	Classes	Flood	Non-flood	Row total	UA(%)
	Flood	10,151	11,434	21,585	47.0
	Non-flood	1,670	38,239	39,909	95.8
	Column total	11,821	49,673	61,494	
	PA (%)	85.9	77.0	OA(%)	78.7
				Kappa(%)	50.6
VH γ^0 (3/1) NF	Classes	Flood	Non-flood	Row total	UA(%)
	Flood	9,907	11,072	20,979	47.2
	Non-flood	1,914	38,601	40,518	95.3
	Column total	11,821	49,673	61,494	
	PA (%)	83.8	77.7	OA(%)	78.9
				Kappa(%)	47.5
VV γ^0 (3/1) Med	Classes	Flood	Non-flood	Row total	UA(%)
	Flood	10,189	7,154	17,343	58.7
	Non-flood	1,632	42,519	44,151	96.3
	Column total	11,821	49,673	61,494	
	PA (%)	86.2	85.6	OA(%)	85.7
				Kappa(%)	60.9
VH γ^0 (3/1) Med	Classes	Flood	Non-flood	Row total	UA(%)
	Flood	9,483	7,410	16,893	56.1
	Non-flood	2,338	42,263	44,601	94.8
	Column total	11,821	49,673	61,494	
	PA (%)	80.2	85.1	OA(%)	84.1
				Kappa(%)	56.5

in land-cover classification that uses remotely sensed data. This method can perform well with relatively small training datasets compared with other commonly used learning classifiers [34], [35]. We utilized LIBSVM [36] as an SVM library to classify nonfloods and floods using the same sampling dataset that was used for automatic thresholding. LIBSVM supports C-support vector classification [36] with a radial basis function as a kernel function [35], [36]. The hyperparameters (cost and gamma) of the SVM were tuned via a grid search [34] with stratified *K*-fold cross validation [36], [37] in this analysis.

Table X lists the number of training samples and hyperparameters determined using the same γ^0 samples used in our proposed method to create Figs. 12 (nonfiltered samples) and 13 (median-filtered samples). Fig. 16 shows the SVM-classified images, and Table XI presents the confusion matrices for the nonflooded and flooded classification results using the SVM classifier with nonfiltered and median-filtered γ^0 data. By comparing Fig. 16 and Table XI with our proposed method results, we can conclude that an SVM classifier did not improve the results.

VI. CONCLUSIONS AND FUTURE WORK

In this study, we attempted to extract the flooded area from a rice paddy field in Bojongsoang, Indonesia, during the significant inundation that occurred from the end of February to the beginning of March 2018. Sentinel-1 *C*-band SAR data that were acquired before and during the flooding events were used to extract the flooded areas. We also used the NDWI created from the PlanetScope images to evaluate the classification accuracy for the nonflooded and flooded fields.

The results indicate that the proposed method can determine thresholds that can be used to classify the nonflooded and flooded areas in rice paddy fields. The thresholds of VV γ^0 were found to divide the nonflooded and flooded areas of rice paddy fields with slightly better accuracy than VH γ^0 in terms of correlation ratios and discriminant accuracies. The classification accuracy reached 84.7% for VV and 80.6% for VH, including the errors that resulted from time differences in the data acquisition. We also recognized improvements resulting from the use of speckle-reducing filters. The comparison of two speckle-reducing filters, the Lee filter and the median filter, indicated that the median-filtered γ^0 outperformed the Lee-filtered γ^0. The overall classification accuracy improved by approximately 5%, reaching 89.3% for VV and 86.0% for VH.

Since knowledge about the growth stage of the rice in a paddy field is necessary in order to generate the accurate assessment of the damage caused by flooding, the growth stage of the rice is also investigated in combination with the new method of flood detection.

ACKNOWLEDGMENT

REFERENCES

[1] SATREPS Project. Accessed on: Feb. 9, 2021. [Online]. Available: https://www.jst.go.jp/global/english/kadai/h2804_indonesia.html

[2] O. Caasi, C. Hongo, A. Suryaningsih, S. Wiyono, K. Homma, and M. Shishido, "Relationships between bacterial leaf blight and other diseases based on field assessment in Indonesia," *Trop. Agriculture Develop.*, vol. 63, no. 3, pp. 113–121, 2019.

[3] H. Wakabayashi *et al.*, "Flooded area extraction of rice paddy field in Indonesia using Sentinel-1 SAR data," *Int. Arch. Photogramm., Remote Sens. Spatial Inf. Sci.*, vol. XLII-3/W7, pp. 73–76, 2019.

[4] R. Yudarwati, C. Hongo, G. Sigit, B. Barus, and B. Utoyo, "Bacterial leaf blight detection in rice crops using ground-based spectroradiometer data and multi-temporal satellites images," *J. Agricultural Sci.*, vol. 12, no. 2, pp. 38–49, 2020.

[5] J.-B. Henry, P. Chastanet, K. Fellah, and Y.-L. Desnos, "Envisat multi-polarized ASAR data for flood mapping," *Int. J. Remote Sens.*, vol. 27, no. 10, pp. 1921–1929, 2006.

[6] S. Martinis, A. Twele, and S. Voigt, "Towards operational near real-time flood detection using a split-based automatic thresholding procedure on high resolution TerraSAR-X data," *Natural Hazards Earth Syst. Sci.*, vol. 9, no. 2, pp. 303–314, 2009.

[7] M. Ohki *et al.*, "Flood area detection using ALOS-2 PALSAR-2 data for the 2015 heavy rainfall disaster in the Kanto and Tohoku area," *J. Remote Sens. Soc. Jpn.*, vol. 36, no. 4, pp. 348–359, 2016.

[8] J. H. Reksten, A.-B. Salberg, and R. Salberg, "Flood detection in Norway based on Sentinel-1 SAR imagery," *Int. Arch. Photogramm. Remote Sens. Spatial Inf. Sci.*, vol. XLII-3/W8, pp. 349–355, 2019.

[9] A. Refice *et al.*, "SAR and InSAR for flood monitoring: Examples with COSMO-SkyMed data," *IEEE J. Sel. Topics Appl. Earth Observ. Remote Sens.*, vol. 7, no. 7, pp. 2711–2722, Jul. 2014.

[10] L. Pulvirenti, M. Chini, N. Pierdicca, and G. Boni, "Use of SAR data for detecting floodwater in urban and agricultural areas: The role of the interferometric coherence," *IEEE Trans. Geosci. Remote Sens.*, vol. 54, no. 3, pp. 1532–1544, Mar. 2016.

[11] H.-G. Sohn, Y.-S. Song, and G.-H. Kim, "Detecting water area during flood event from SAR image," in *Proc. Int. Conf. Comput. Sci. Appl.*, 2005, vol. 3481, pp. 771–780.

[12] A. Dasgupta, S. Grimaldi, R. Ramsankaran, and J. P. Walker, "Optimized GLCM-based texture features for improved SAR-based flood mapping," in *Proc. IEEE Int. Geosci. Remote Sens. Symp.*, 2017, pp. 3258–3261.

[13] R. M. Haralick, K. Shanmugam, and I. Dinstein, "Textural features for image classification," *IEEE Trans. Syst., Man, Cybern.*, vol. SMC-3, no. 6, pp. 610–621, Nov. 1973.

[14] F. S. Hanidya, "Flood vulnerability analysis in Bojongsoang district, Bandung regency," Graduation Res. Land Resour. Manage. Study Program, IPB Univ., Bogor, Indonesia, 2018.

[15] Sentinel-1 Acquisition Mode. Accessed on: Apr. 10, 2021 [Online]. Available: https://sentinel.esa.int/web/sentinel/user-guides/sentinel-1-sar/acquisition-modes/.

[16] F. De Zan and A. M. Guarnieri, "TOPSAR: Terrain observation by progressive scans," *IEEE Trans. Geosci. Remote Sens.*, vol. 44, no. 9, pp. 2352–2360, Sep. 2006.

[17] IW GRD Resolutions. Accessed on: Apr. 10, 2021. [Online]. Available: https://sentinel.esa.int/web/sentinel/technical-guides/sentinel-1-sar/products-algorithms/level-1-algorithms/ground-range-detected/iw/

[18] Sentinel-1 Product Definition. Accessed on: Apr. 10, 2021. [Online]. Available: https://sentinels.copernicus.eu/documents/247904/1877131/Sentinel-1-Product-Definition

[19] Planet Satell. Imag. Arch. [Online]. Available: https://www.planet.com/products/planet-imagery/

[20] Planet Imag. Prod. Specifications. Accessed on: Apr. 10, 2021. [Online]. Available: https://assets.planet.com/docs/Planet_Combined_Imagery_Product_Specs_letter_screen.pdf

[21] S. Martinis, J. Kersten, and A. Twele, "A fully automated TerraSAR-X based flood service," *ISPRS J. Photogramm. Remote Sens.*, vol. 104, pp. 203–212, 2015.

[22] L. Pulvirenti, M. Chini, N. Pierdicci, L. Guerriero, and P. Ferrazzoli, "Flood monitoring using multi-temporal COSMO-SkyMed data: Image segmentation and signature interpretation," *Remote Sens. Environ.*, vol. 115, no. 4, pp. 990–1002, 2011.

[23] M. Ohki *et al.*, "Flood area detection using PALSAR-2 amplitude and coherence data: The case of the 2015 heavy rainfall in Japan," *IEEE J. Sel. Topics Appl. Earth Observ. Remote Sens.*, vol. 12, no. 7, pp. 2288–2298, Jul. 2019.

[24] D. C. Mason, I. J. Davenport, J. C. Neal, G. J.-P. Schumann, and P. D. Bates, "Near real-time flood detection in urban and rural areas using high-resolution synthetic aperture radar images," *IEEE Trans. Geosci. Remote Sens.*, vol. 50, no. 8, pp. 3041–3052, Aug. 2012.

[25] M. Chini, R. Hostache, L. Giustarini, and P. Matgen, "A hierarchical split-based approach for parametric thresholding of SAR images: Flood inundation as a test case," *IEEE Trans. Geosci. Remote Sens.*, vol. 55, no. 12, pp. 6975–6988, Dec. 2017.

[26] J. Kittler and J. Illingworth, "Minimum error thresholding," *Pattern Recognit.*, vol. 19, no. 1, pp. 41–47, 1986.

[27] N. Otsu, "A threshold selection method from gray-level histogram," *IEEE Trans. Syst., Man, Cybern.*, vol. SMC-9, no. 1, pp. 62–66, Jan. 1979.

[28] ESA Sentinel Toolboxes, Accessed on: Apr. 10, 2021. [Online]. Available: https://sentinel.esa.int/web/sentinel/toolboxes

[29] D. Small, "Flattening gamma: Radiometric terrain correction for SAR imagery," *IEEE Trans. Geosci. Remote Sens.*, vol. 49, no. 8, pp. 3081–3093, Aug. 2011.

[30] S. K. McFeeters, "The use of the normalized difference water index (NDWI) in the delineation of open water features," *Int. J. Remote Sens.*, vol. 17, no. 7, pp. 1425–1432, 1996.

[31] R. A. Fisher, "The use of multiple measurements in taxonomic problems," *Ann. Eugenics*, vol. 7, no. 2, pp. 179–188, 1936.

[32] J.-S. Lee, "Refined filtering of image noise using local statistics," *Comput. Graph. Image Process.*, vol. 15, no. 4, pp. 380–389, 1981.

[33] C. Cortes and V. Vapnik, "Support-vector networks," *Mach. Learn.*, vol. 20, pp. 273–297, 1995.

[34] A. E. Maxwell, T. A. Warner, and F. Fang, "Implementation of machine-learning classification in remote sensing: An applied review," *Int. J. Remote Sens.*, vol. 39, no. 9, pp. 2784–2817, 2018.

[35] G. Mountrakis, J. Im, and C. Ogole, "Support vector machines in remote sensing: A review," *ISPRS J. Photogramm. Remote Sens.*, vol. 66, pp. 247–259, 2011.

[36] C.-C. Chang and C.-J. Lin, "LIBSVM: A library for support vector machines," *ACM Trans. Intell. Syst. Technol.*, vol. 2, no. 3, 2011, Art. no. 27.

[37] C. A. Ramezan, T. A. Warner, and A. E. Maxwell, "Evaluation of sampling and cross-validation tuning strategies for regional-scale machine learning classification," *Remote Sens.*, vol. 11, no. 2, 2019, Art. no. 185.

Hiroyuki Wakabayashi (Member, IEEE) received the B.S. and M.S. degrees in electronic engineering and the Ph.D. degree in applied physics, all from Hokkaido University, Hokkaido, Japan, in 1981, 1983, and 1996, respectively.

In 1983, he joined the National Space Development Agency in Japan (NASDA, currently JAXA). He worked on the data processing and cal/val systems for JERS-1, from 1986 to 1991, and the ALOS/PALSAR conceptual design from 1994 to 1999. From 1999 to 2006, he was a Research Scientist with Earth Observation Research Center and engaged in polarimetric synthetic aperture radar (SAR) research. From 2001 to 2003, he stayed with Syowa Station, where he was in charge of SAR data processing and analysis for sea ice monitoring. Since April 2006, he has been with the College of Engineering, Nihon University, Fukushima, Japan, where he is currently a Professor of Computer Science.

Dr. Wakabayashi is a member of IEICE, the Remote Sensing Society of Japan, the Japan Society of Photogrammetry and Remote Sensing, the Japanese Society of Snow and Ice, and the 43rd Japanese Antarctic Research Expedition.

Chiharu Hongo received the Ph.D. degree in agricultural remote sensing from Chiba University, Chiba, Japan, in 1994.

She is an Associate Professor with the Integrated Research Field of Remote Sensing Division, Center for Environmental Remote Sensing, Chiba University, Japan, where she has both teaching and research responsibilities.

Dr. Hongo has been involved in research and development to utilize remote sensing in the agriculture area for about 30 years. She is a Pioneer Researcher in area of the agricultural remote sensing in Japan. Furthermore, she has extensive experiences in leading various research projects of Government and public organizations and also private companies. She is currently conducting a Science and Technology Research Partnership for Sustainable Development Project with Indonesian partners as a project leader whose title is the "Development and Implementation of New Damage Assessment Process in Agricultural Insurance as Adaptation to Climate Change for Food Security."

Takahiro Igarashi received the B.E. and M.E. degrees in computer science in 2019 and 2021, respectively, from Nihon University, Fukushima, Japan, where he is currently working toward the Ph.D. degree in computer science at Nihon University.

His research interests include machine learning techniques applied to high-resolution optical and microwave remote sensing data.

Yoshihiro Asaoka received the B.E., M.E., and Ph.D. degrees in civil engineering from Tohoku University, Miyagi, Japan, in 2000, 2002, and 2005, respectively.

From 2005 to 2006, he was a Postdoctoral Researcher with Forestry and Forest Products Research Institute, Japan, from 2006 to 2009, the Central Research Institute of Electric Power Industry, Japan, and from 2009 to 2015, the Graduate School of Engineering, Tohoku University. Since 2015, he has been with the College of Engineering, Nihon University, Fukushima, Japan. His current research interests include climate change impacts of water resources in snow-covered areas and glacierized areas, and climate change adaptation in water disasters.

Boedi Tjahjono received the bachelor's degree in geography and geomorphology from Gadjah Mada University, Yogyakarta, Indonesia, in 1986, the postgraduate degree in "geographical landscape analysis for Indonesian resources with the emphasis on applied geomorphological survey" from International Institute for Aerospace Survey and Earth Sciences, Enschede, The Netherlands, in 1991, the master's degree (Diplome d'Etude Approfondie) in geography from Université de Nancy II, Nancy, France, in 1993, and the Doctorate degree in geography from Université Blaise Pascal, Clermont-Ferrand II, Clermont-Ferrand, France, in 1998.

Since 1987, he has been teaching with IPB University, Bogor, Indonesia, in the fields of geomorphology, geographic information science, and natural disasters and mitigation, and since 2011, he has been assisting the Indonesian Ministry of Environment and Forestry in drafting and mapping Ecoregions and Environmental Carrying Capacity throughout Indonesia. In 2017, he joined the research collaboration project with the Japanese Government "SATREPS" entitled "Development and Implementation of New Damage Assessment Process in Agricultural Insurance as Adaptation to Climate Change for Food Security" as a part of the IPB University team.

Intan Rima Ratna Permata received the bachelor's degree in chemistry from Padjadjaran University, Bandung, Indonesia, in 2011.

In 2014, she was a Plant Pest Organism Controller with "Food Crops and Horticulture Protection Center," a part of the "West Java Province Food Crops and Horticulture Service." Since 2017, she has been with a collaborative research project with the Japanese Government "SATREPS" entitled "Development and Implementation of a New Damage Assessment Process in Agricultural Insurance as Climate Change Adaptation for Food Security" as a part of the West Java Province Food Crops and Horticulture Service team.